Extreme Materials 2 (2026) 47–57

Contents lists available at ScienceDirect

Extreme Materials

journal homepage: www.keaipublishing.com/en/journals/extreme-materials/

Design of amorphous/nanocrystalline turing structures in ZrO_2/C nanofibers for enhanced microwave absorption performance

Yaqing Li[a], Cheng Fang[a,*], Bei Cai[a], Xu Long[a], Wei Xie[a], Huimin Xiang[a], Hailong Wang[a], Yanchun Zhou[b,*]

[a] School of Materials Science and Engineering, Zhengzhou University, Zhengzhou 450001, China
[b] Suzhou National Laboratory, Suzhou 215000, China

ARTICLE INFO

Keywords:
ZrO_2/C nanofibers
Electromagnetic wave absorption
Turing structure
Amorphous/nanocrystalline

ABSTRACT

With the growing prominence of electromagnetic pollution, the development of lightweight, flexible, and highly efficient electromagnetic wave (EMW) absorption materials has become an important research focus. Inspired by biological Turing structures, this study successfully prepares novel flexible ZrO_2/C nanofibers with a spotted reaction-diffusion pattern via a controlled oxidation strategy from preformed ZrC/C nanofibers. The ZrO_2/C nanofibers sample contains ZrO_2 particles embedded within a carbon matrix, which contributes to the formation of numerous heterogeneous interfaces. Furthermore, both the ZrO_2 and carbon matrix exhibit a mixed amorphous-nanocrystalline structure, thereby enhancing interfacial diversity and density. The ZrO_2/C Turing structural characteristic enhances impedance matching in the nanofibers and significantly improves the polarization loss capability. The obtained novel nanofibers achieve a minimum reflection loss of −59.20 dB, a maximum effective absorption bandwidth of 5.84 GHz, and require a matching thickness of only 2.39 mm. Computer simulation technology (CST) simulations indicate a maximum radar cross-section reduction of 34.94 dB m^2, highlighting the material' s radar stealth capability. The study provides a new strategy for designing lightweight and high-performance fiber-based EMW absorption materials.

1. Introduction

With the rapid advancement of modern communication technologies and electronic devices, issues of electromagnetic wave (EMW) interference and pollution have become increasingly prominent. Strong electromagnetic interference not only disrupts the normal operation of equipment, but may also lead to critical system failures [1]. The development of novel microwave absorption materials with superior EMW absorption performance has emerged as a key research direction in this field [2]. Among various candidate materials, one-dimensional carbon nanofibers are considered promising for next-generation lightweight and broadband absorption systems due to their low density, high specific surface area and excellent mechanical flexibility. However, the inherently high electrical conductivity of carbon nanomaterials often results in poor impedance matching with free space [3]. This impedance mismatch hinders the efficient penetration of EMWs into the material, thereby restricting any further enhancement of its absorption performance. Consequently, incorporating dielectric components into the carbon matrix is considered an effective strategy to mitigate this issue and improve the overall wave-absorbing properties.

Zirconia (ZrO_2) exhibits favorable wave-transparent properties and relatively low electrical conductivity [4]. It is believed that the introduction of ZrO_2 into the carbon nanofibers matrix can effectively modulate the electrical conductivity and alleviate the impedance mismatch. Furthermore, the heterogeneous interfaces formed between the different phases can significantly enhance interfacial polarization, leading to improved EMW dissipation. Wang *et al.* conducted a systematic investigation on the microwave absorption performance of ZrO_2/C bulk composite. A minimum reflection loss (RL_{min}) of −37.8 dB was achieved at a matching thickness of 3 mm, with an effective absorption bandwidth (*EAB*) reaching 7.3 GHz, demonstrating the potential of ZrO_2/C systems in EMW absorption [5]. Notably, Sun *et al.* fabricated ZrO_2/C nanofibers via electrospinning using a precursor system containing ZrO_2 powder and polyacrylonitrile [6]. The obtained

Peer review under the responsibility of Editorial Board of Extreme Materials.
* Corresponding authors.
E-mail addresses: fangcheng@zzu.edu.cn (C. Fang), yczhou@alum.imr.ac.cn (Y. Zhou).

https://doi.org/10.1016/j.exm.2026.100022
Received 15 September 2025; Received in revised form 15 November 2025; Accepted 3 January 2026
Available online 17 March 2026
3050-628X/© 2026 The Authors. Publishing services by Elsevier B.V. on behalf of KeAi Communications Co. Ltd. This is an open access article under the CC BY license (http://creativecommons.org/licenses/by/4.0/).

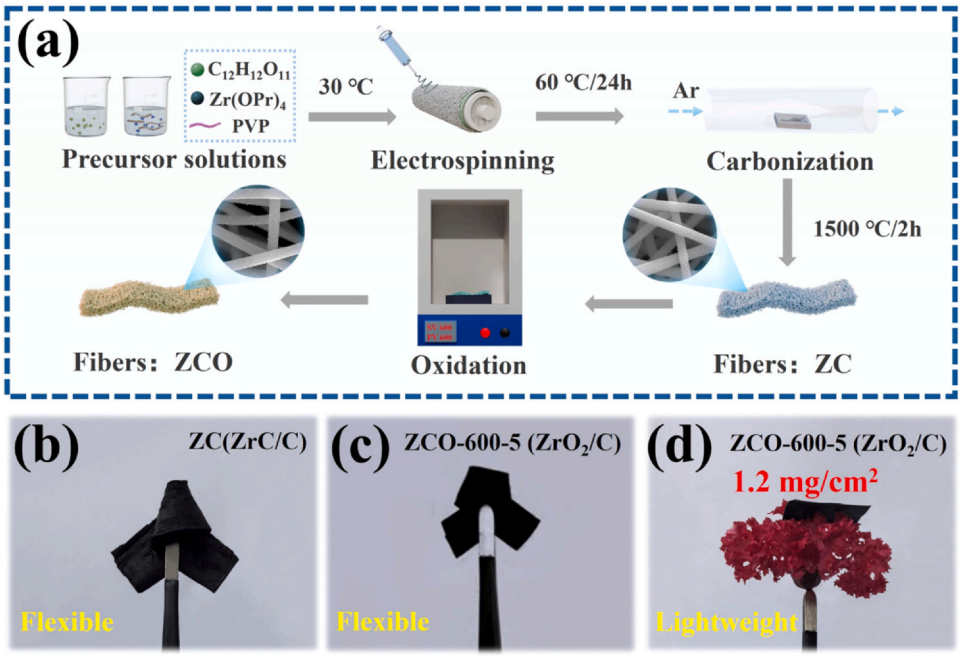

Fig. 1. Synthesis process and macroscopic morphology of ZCO nanofibers. (a) The schematic diagram of the preparation process of ZC and ZCO. (b) The surface density of ZCO-600–5. (c-d) The macroscopic morphology of the ZCO-600–5 after mechanical folding.

nanofibers exhibited an absorption-dominated electromagnetic interference shielding mechanism, thereby substantiating the potential of such a component combination in microwave absorption applications. However, achieving uniform dispersion of ZrO_2 and carbon through traditional mixing approaches remains challenging, which leads to limited and non-uniformly distributed heterogeneous interfaces. This inhomogeneity restricts the full exploitation of interfacial polarization and ultimately limits the enhancement of EMW dissipation. Thus, achieving precise control over the construction of ZrO_2 and carbon phases and optimizing their interfacial structures within nanofiber systems are essential for maximizing the performance of ZrO_2/C nanofibers.

It has come to light that certain non-equilibrium thermodynamic processes based on reaction-diffusion mechanisms can lead to the formation of heterostructures with non-uniformly distributed interfaces within the resulting materials. This phenomenon is analogous to the formation of Turing patterns widely observed in nature, wherein the spontaneous periodic spatial organization of components gives rise to numerous heterogeneous microdomains and interfaces [7]. In recent years, it has been demonstrated that carbothermal reduction reactions can be employed to fabricate nanofibers exhibiting spot-like Turing patterns. For example, Song *et al.* and Tao *et al.* successfully prepared ZrC/C nanofibers via electrospinning and carbothermal reduction methods, respectively, both of which exhibited distinct spot-like patterns within the nanofibers [8,9]. In these structures, island-like ZrC nanoparticles were uniformly embedded in a continuous carbon matrix, creating abundant heterogeneous interfaces. Such Turing-inspired structures served to enhance interfacial polarization, facilitate charge accumulation and migration at the interfaces, and substantially improved the polarization loss capability for EMW absorption [10]. However, both ZrC and C are electrically conductive, which may result in poor impedance matching with free space. Thus, developing a precise process to transfer electrically conductive ZrC into dielectric ZrO_2 while preserving the spot-like Turing structure is highly desirable. To achieve such a goal, ZrO_2/C nanofibers with biomimetic Turing-type architectures were constructed through a controlled oxidation process of the as-prepared ZrC/C nanofibers in this work. This approach enables uniform dispersion and interfacial coupling between the ZrO_2 and carbon matrix within the nanofibers. Furthermore, by optimizing the oxidation temperature and duration, graphitization of the carbon matrix can be effectively suppressed, thereby preserving the mechanical flexibility of the nanofibers.

As we will show in the following sections, ZrO_2/C nanofibers featuring a multi-interfacial Turing-like structure were successfully prepared through controlled oxidation of pre-fabricated ZrC/C precursor nanofibers. The effects of oxidation conditions on the microstructure and microwave absorption properties of the ZrO_2/C nanofibers were systematically investigated. The EMW absorption mechanisms of the Turing-type structured nanofibers were also discussed.

2. Experiments and methods

2.1. Preparation of ZrC/C and ZrO_2/C nanofibers

ZrC/C nanofibers were synthesized via a carbothermal reduction process. A carbon source solution was first prepared by dissolving sucrose ($C_{12}H_{22}O_{11}$, Adamas) and polyvinylpyrrolidone (as a spinning aid) in N,N-dimethylformamide under stirring at 80 ℃ for 2 h. Separately, a zirconium precursor solution was formulated by mixing Zirconium (IV) n-propoxide with anhydrous ethanol and acetylacetone (chelating agent) in a volume ratio of 4:3:1, followed by stirring at room temperature for 2 h. The two solutions were then combined and stirred for 8 h at room temperature to obtain a homogeneous spinnable sol. The precursor nanofibers were produced by electrospinning of the resultant sol, which were subsequently stabilized at 350 ℃ and then carbonized at 1500 ℃ to yield ZrC/C nanofibers, denoted as ZC. The reaction process within ZC nanofibers is clearly depicted in Fig. S4.

The transformation of ZrC/C nanofibers into ZrO_2/C nanofibers was achieved through an in-situ oxidation process. To investigate the effect of oxidation temperature, ZC nanofibers were oxidized at 500 ℃, 600 ℃ and 700 ℃ for 5 min, yielding samples designated as ZCO-500–5, ZCO-600–5 and ZCO-700–5, respectively. To further examine the influence of oxidation time, isothermal treatments were conducted at 600 ℃ for 3, 5 and 10 min, with the resulting nanofibers labeled accordingly as ZCO-600–3, ZCO-600–5 and ZCO-600–10 (Fig. S5). The schematic diagram of the preparation process of ZC and ZCO nanofibers, as well as the macroscopic morphology of the prepared nanofibers, are shown in Fig. 1.

2.2. Methods

Simultaneous thermal analysis (TG-DSC, NETZSCH STA 449F3) was conducted in air atmosphere with the temperature raised from room temperature to 1100 ℃ at a heating rate of 7 ℃/min. The crystal structures of the ZC and ZCO nanofibers were analyzed by X-ray diffraction (XRD, D8 Advance, Bruker, Germany). The surface chemical composition of the nanofibers was characterized using X-ray photoelectron spectroscopy (XPS, Thermo Scientific K-Alpha). Microstructural and morphological features were examined in a scanning electron microscope (SEM, JSM-IT800, JEOL, Japan). Raman spectroscopy (HORIBA LabRam HR Evolution, Japan) was employed to evaluate the structural order and defects of the carbon phase within the surface region of the nanofibers. To obtain detailed crystallographic information, focused ion beam (FIB, Thermo Scientific Scios 2) was used to prepare lamellae from fiber fractures, which were then analyzed by transmission electron microscopy (TEM, JEM-F200, JEOL, Japan), high-resolution TEM (HRTEM) and aberration-corrected TEM (AC-TEM, Thermo Scientific Spectra Ultra). Moreover, the electromagnetic parameters in the frequency range of 2.0–18.0 GHz were measured using a vector network analyzer (Agilent N5244A, Keysight Technologies, Inc.). For these measurements, the fiber samples were homogeneously mixed with wax at a concentration of 5 wt% and pressed into toroidal-shaped specimens with an outer diameter of 7.00 mm and an inner diameter of 3.04 mm.

3. Results and discussion

3.1. Structural investigation of the ZrC/C and ZrO_2/C nanofibers

The XRD pattern of the ZC nanofibers is presented in Fig. 2a, which clearly reveals the presence of a cubic ZrC phase (PDF#97–061–9153). To further investigate the chemical composition and elemental valence states, XPS analysis was conducted on the ZC nanofibers. Fig. S1 shows the XPS survey scan of ZC nanofibers. The C 1 *s* spectrum (Fig. 2d) could be deconvoluted into four characteristic peaks, corresponding to C-C, C-O, C═O and Zr-C bonds, respectively [11,12]. The O 1 *s* spectrum (Fig. 2e) indicates the presence of Zr-O (530.5 eV), O-C (532.0 eV) and O═C (532.9 eV) bonds, which can be assigned to lattice oxygen, surface oxygen vacancies and adsorbed oxygen species, respectively [13,14]. Furthermore, the XPS spectrum of Zr 3*d* (Fig. 2f) confirms that the primary chemical bonds on the surface consist of Zr-C and Zr-O bonds. Fig. 2c shows the Raman spectra of both ZC and ZCO nanofibers. Two distinct peaks are observed near 1590 cm^{-1} (G-band) and 1340 cm^{-1} (D-band), which are attributed to the highly ordered graphitic lattice and structural defects in carbon materials, respectively. The I_D/I_G intensity ratio is commonly used to evaluate the graphitization degree of carbonaceous materials [15]. The ZC nanofibers exhibit an I_D/I_G ratio of 1.13, which indicates that the fibrous structure consists of amorphous carbon. [16]. To achieve the controlled transformation of ZC nanofibers into ZCO nanofibers, a thorough understanding of the oxidation mechanism is essential. Based on the TG-DSC curves shown in Fig. 2b, the oxidation process of the ZC nanofibers can be divided into four distinct stages [17]. The first stage (25–270 ℃) exhibits a mass loss of approximately 1 wt%, attributed to the evaporation of adsorbed water from the fiber surface. In the second stage (270–433 ℃), a significant mass gain of 19.8% is observed, accompanied by a distinct exothermic peak at 380 ℃ on the DSC curve. This temperature corresponds to the maximum mass gain rate and indicates the occurrence of an exothermic reaction involving the oxidation of ZrC to ZrO_2. The third stage (433–594 ℃) shows a remarkable mass loss of 40.8%, with an exothermic peak at 541 ℃ on the DSC curve coinciding with the sharp mass decrease, resulting from the oxidation of the amorphous carbon matrix. During the fourth stage (594–1100 ℃), the gradual mass loss can be primarily attributed to the slow yet continuous oxidation of the carbon matrix. The relatively low oxidation rate is likely due to the partial protective effect conferred by the ZrO_2. To achieve conversion of ZrC to ZrO_2 while preventing excessive oxidation of the carbon matrix, oxidation temperatures of 500 ℃, 600 ℃ and 700 ℃ were selected for subsequent experiments.

The phase compositions of the ZCO nanofibers after oxidation at different temperatures are shown in Fig. 2a. In the ZCO-500–5 sample, the intensity of the ZrC diffraction peaks exhibits a slight decrease compared to the pristine ZC nanofibers. As the oxidation temperature

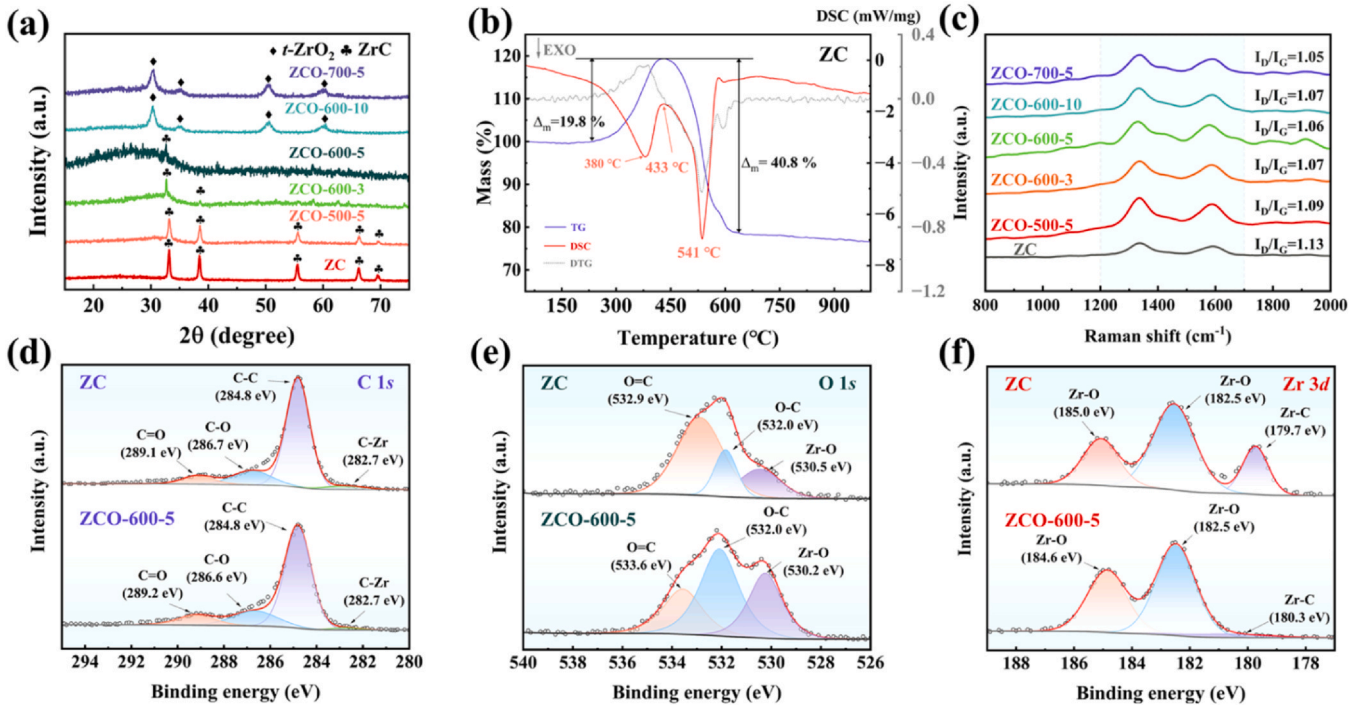

Fig. 2. Phase characterization of the nanofibers. (a) XRD patterns of ZC and ZCO. (b) TG-DSC curves of ZC. (c) Raman spectra of ZC and ZCO. (d) The C 1 *s* spectrum of ZC and ZCO-600–5. (e) The O 1 *s* spectrum of ZC and ZCO-600–5. (f) The Zr 3*d* spectrum of ZC and ZCO-600–5.

increases, the ZCO-600–5 sample is predominantly characterized by an amorphous ZrO_2 phase, with the ZrC peaks significantly weakened and obscured due to a substantial reduction in crystalline content. The ZCO-700–5 sample exhibited distinct and sharp diffraction peaks, which are indicative of the crystallization tendency of ZrO_2 at elevated temperatures. Considering the potentially complex structure of ZCO-600–5, which may comprise both amorphous and nanocrystalline ZrO_2, gradient oxidation experiments with varying durations were conducted at 600 ℃ to further elucidate its phase evolution. The reduction in intensity of the ZrC diffraction peaks is clearly observed in the ZCO-600–3 sample, whereas well-defined crystalline diffraction peaks corresponding to ZrO_2 emerge in the ZCO-600–10 sample. Furthermore, the nearly identical I_D/I_G ratios observed for the ZCO nanofibers (Fig. 2c) indicate that the low-temperature oxidation process exerts minimal influence on the graphitization degree of the carbon matrix. Crystallinity and amorphous content significantly influence the EMW absorption performance of the material. Higher crystallinity tends to enhance the reflection and scattering of EMWs. In contrast, a higher amorphous content generally contributes to improved impedance matching, reducing reflection at the material-air interface and thereby enhancing absorption [18]. Therefore, the ZCO-600–5 sample, with its moderate crystallinity, is considered more conducive to achieving efficient EMW absorption and has been selected as the optimal sample for further investigation in this study.

3.2. Morphological analysis of ZC and ZCO nanofibers

Fig. 3 presents SEM images of the pristine ZC nanofibers and the ZCO nanofibers obtained under different oxidation conditions. The ZC nanofibers exhibit a smooth surface and an average diameter of approximately 550 nm (Fig. 3a). As the oxidation proceeds, the ZrC phase gradually transforms into ZrO_2, accompanied by the formation of micro-protrusions on the nanofibers surface. Meanwhile, the carbon matrix is progressively consumed through oxidation, leading to a gradual reduction in fiber diameter (Fig. S2). The oxidation degree plays a decisive role in determining the final microstructure. For instance, ZCO-600–10 nanofibers (Fig. 3e) experienced excessive oxidation, which resulted in substantial depletion of the carbon matrix. As a result, the fiber diameter was significantly reduced to 470 nm, and the surface became entirely covered with coarse ZrO_2 particles. This structural evolution would disrupt the original conductive network, thereby adversely affecting the microwave absorption performance. Among all the samples, ZCO-600–5 nanofibers (Fig. 3d) exhibits the most desirable morphological characteristics. Its surface displays uniformly distributed and moderately sized micro-protrusions (Fig. S3), which are beneficial for enhancing multiple reflections and scattering of EMWs. Therefore, the ZCO-600–5 sample, which exhibits a combination of moderate crystallinity and favorable morphology, is regarded as the most suitable candidate for efficient EMW absorption and has been chosen for further investigation in this study.

The microstructure of the ZC nanofibers was thoroughly characterized using HRTEM. The high-resolution image in Fig. 4a and the corresponding EDS results in Fig. 4e reveal that the ZC nanofibers consist of a carbon matrix with embedded crystalline ZrC phases. The ZrC nanoparticles are dispersed as irregular speckles within the nanofibers, forming a Turing-like pattern. The formation of this Turing-type structure can be attributed to a diffusion-reaction dominated phase separation mechanism during the carbonization of the precursor. During the pyrolysis process, the different diffusion rates of the carbon source and zirconium lead to the spontaneous formation of periodic distributions of ZrC nanoparticles within the continuous carbon phase [19]. Furthermore, a detailed analysis was conducted on the grains dispersed in the nanofibers. As shown in Fig. 4b, the grains exhibit a typical “core-rim” architecture, comprising a crystallized core and an outer transition layer. Fig. 4c provides a detailed view of the edge region of a grain, where a distinct difference in crystallinity is evident between the core and the rim. The low-crystallinity rim layer measures approximately 2.51 nm in thickness [20]. Lattice fringes visible in the high-resolution image of the core region indicate the feature of ZrC (Fig. 4d). According to the EDS mapping results of the grain (Fig. 4f), the intensity of the Zr signal is significantly lower in the rim layer than in the core, while carbon remains relatively uniformly distributed. This suggests that the transition

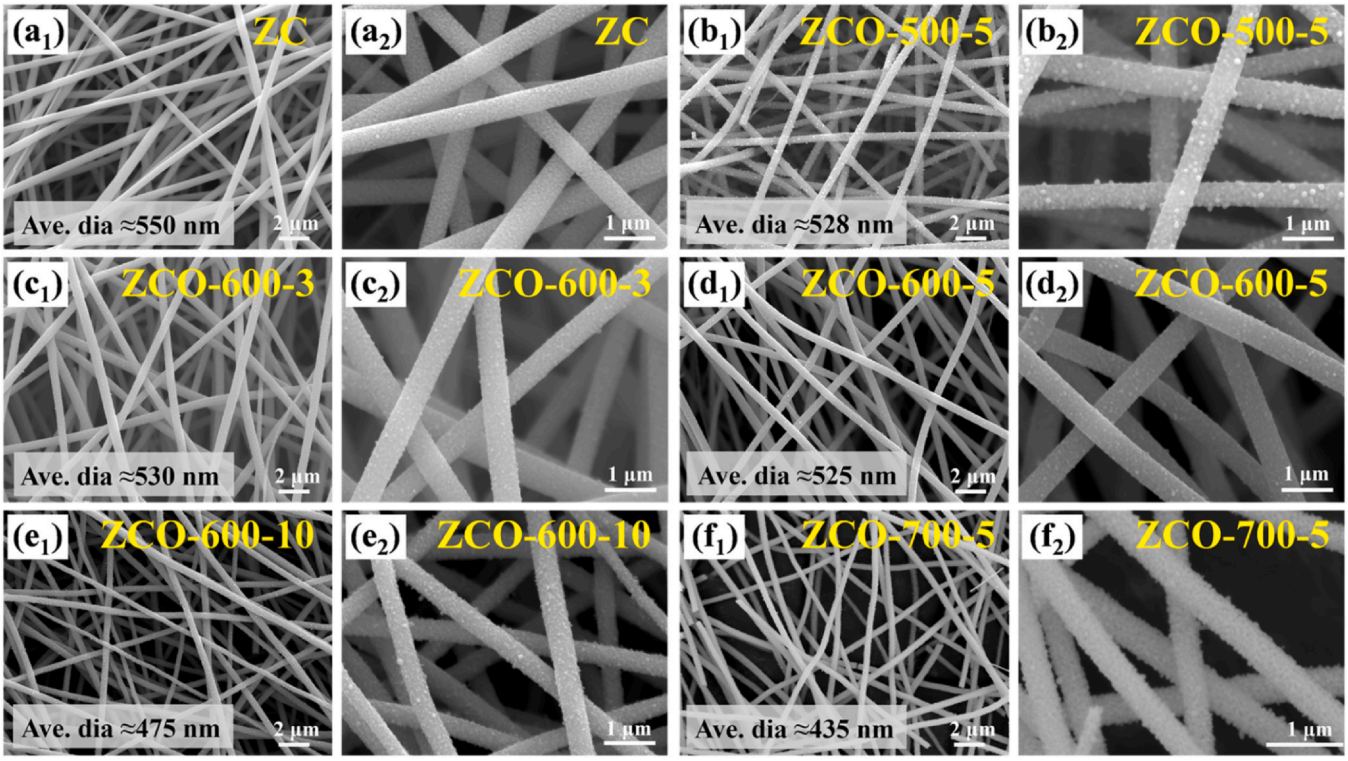

Fig. 3. SEM images of ZC nanofibers and ZCO nanofibers. (a) ZC. (b) ZCO-500–5. (c) ZCO-600–3. (d) ZCO-600–5. (e) ZCO-600–10. (f) ZCO-700–5.

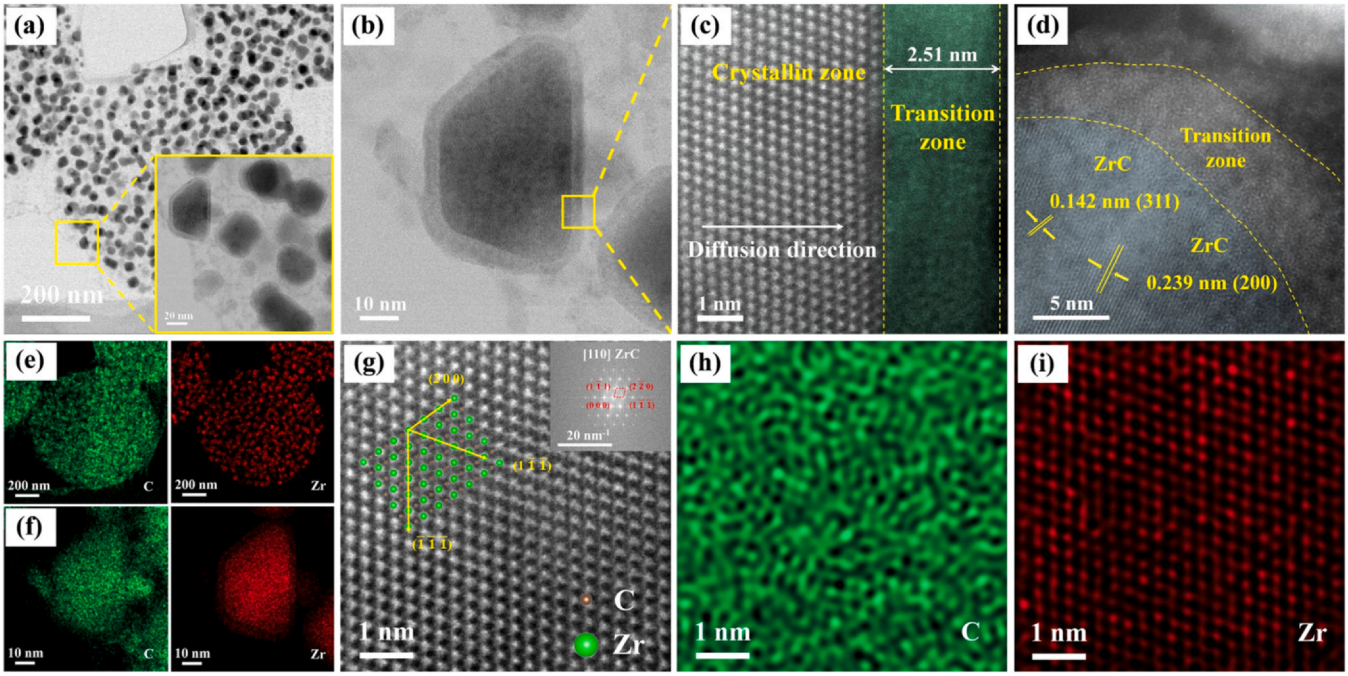

Fig. 4. Microstructure and elemental analysis of ZC nanofibers. (a) Cross-sectional microstructure of ZC. (b)-(c) STEM diagram of ZC. (d) The microstructure at the edge of the ZrC particle. (e) EDS mappings of region (a). (f) EDS mappings of region (b). (g) A high magnification of HAADF-STEM image in the crystallin region of (c). (h)-(i) Atomic resolution EDS mappings of (g).

layer is likely composed of low-crystallinity ZrC and amorphous carbon. Fig. 4g presents a HAADF-STEM image of the core region, where bright spots correspond to Zr atomic columns and dark regions represent carbon atoms [21,22]. The STEM-EDS elemental mappings in Fig. 4h, i corroborate the distribution of carbon and zirconium at the atomic scale, showing high consistency with the ZrC crystal structure. The "core-rim" structure of individual particles and the Turing patterns with the nanofibers both originate from the non-equilibrium growth process. The different diffusion rates not only determine the morphology of the individual ZrC-based particles but also drive the formation of the unique Turing-type architecture of ZC nanofibers.

Further analysis was performed on the morphology and microstructure of the ZCO-600–5 nanofibers obtained through oxidation of the ZC nanofibers. As shown in the bright-field image (Fig. 5a), the resulting ZCO nanofibers exhibit a nanofibers morphology with an average diameter of approximately 440 nm, covered with numerous particulate protrusions on the surface. EDS elemental mapping (Fig. 5b) confirms the homogeneous distribution of Zr and O elements within the amorphous carbon matrix [23]. HRTEM images (Fig. 5c and d) clearly reveal the presence of tetragonal ZrO_2 (*t*-ZrO_2) crystalline regions within the nanofibers. Lattice fringes with a spacing of 0.175 nm, corresponding to the (200) planes of *t*-ZrO_2, are visible in Fig. 5d [19]. The cross-sectional structure (Fig. 5e) indicates that the nanofibers consists of discrete particles embedded in a continuous matrix, inheriting the Turing-type architecture of the ZC precursor (Fig. 5g). Cross-sectional EDS (Fig. 5f) also reveals the nanofibers morphology, with ZrO_2 particles uniformly dispersed in the carbon matrix. High-resolution TEM image shows that the "core-rim" structure originally present in the ZC nanofibers disappears after oxidation (Fig. 5h). The ZrO_2 grains contain both amorphous regions and crystalline *t*-ZrO_2 phases, with lattice spacings of 0.312 nm and 0.187 nm corresponding to the (101) and (112) planes, respectively (Fig. 5i). The continuous carbon matrix also exhibits an amorphous/nanocrystalline mixed structure (Fig. 5k). Quantitative analysis via FFT and autocorrelation function indicates that the crystal lattice order (CLO) [24] values for the ZrO_2 grains and the carbon matrix are 64% and 9%, respectively (Fig. 5j and l), suggesting an abundance of amorphous/nanocrystalline heterogeneous interfaces within the Turing-patterned units.

3.3. Electromagnetic microwave absorption performance

The electromagnetic microwave absorption parameters of the nanofibers before and after oxidation were measured using a vector network analyzer [25]. The reflection loss (*RL*) values under different matching thicknesses were calculated based on transmission line theory and Eqs. (1) and (2):

$$Z_{in} = Z_0 \sqrt{\frac{\varepsilon_r}{\mu_r}} \tanh\left[j\left(\frac{2\pi f d}{c}\right)\sqrt{\varepsilon_r \mu_r}\right] \quad (1)$$

$$RL = 20 \lg \left| \frac{Z_{in} - Z_0}{Z_{in} + Z_0} \right| \quad (2)$$

where Z_{in} denotes the input impedance, Z_0 is the impedance of free space, f is the frequency, c is the speed of light and d is the sample thickness. A lower *RL* value indicates stronger microwave absorption capability. An *RL* value of −10 dB is generally regarded as the effective absorption threshold, implying that 90% of the incident wave is absorbed [26]. The corresponding frequency range is defined as the effective absorption bandwidth (*EAB*). An ideal microwave absorber should exhibit a more negative *RL* value and a wider *EAB*. Fig. 6a-f present the EMW absorption properties of ZC nanofibers and ZCO nanofibers prepared under different oxidation temperatures and durations with a loading ratio of 5 wt%. As shown in Fig. 6a, the ZC nanofibers show limited absorption performance, with a minimum reflection loss (RL_{min}) of only −9.45 dB at a thickness of 4.99 mm. In contrast, the ZCO-600–5 sample, as anticipated from earlier structural analysis, demonstrates outstanding absorption characteristics. It achieves an RL_{min} of −59.20 dB at a matching thickness of 2.39 mm, along with a maximum effective absorption bandwidth (EAB_{max}) of 5.84 GHz (covering 11.48–17.32 GHz). Samples subjected to either insufficient or excessive oxidation failed to attain comparable performance.

In EMW absorption, the complex permittivity ε_r ($\varepsilon_r = \varepsilon' - j\varepsilon''$) and complex permeability μ_r ($\mu_r = \mu' - j\mu''$) play critical roles. The real parts (ε' and μ') represent the ability to store electromagnetic energy, while the imaginary parts (ε'' and μ'') reflect the dissipation capability. The dielectric

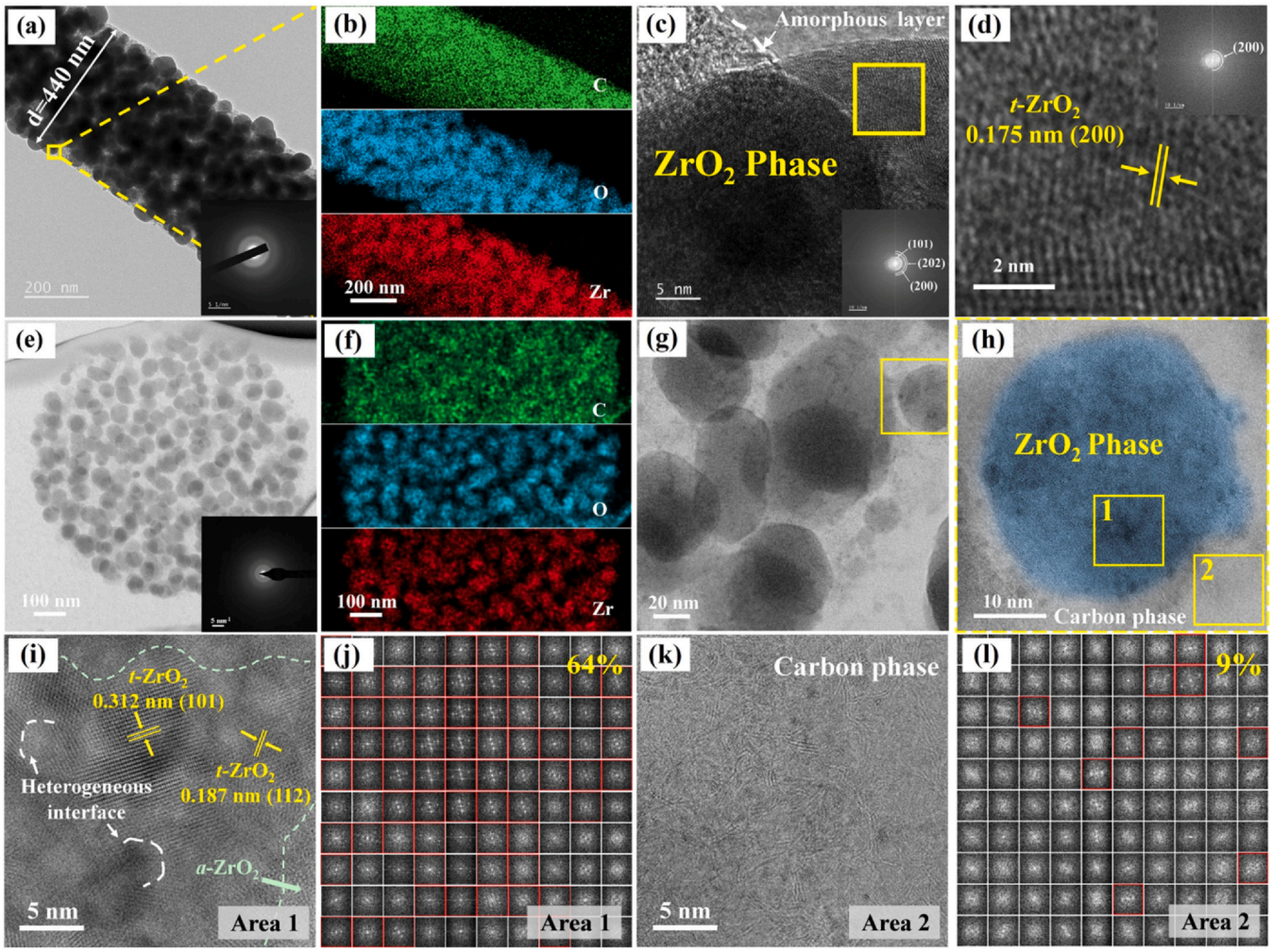

Fig. 5. Microstructure, elemental analysis, and crystallinity analysis of ZCO nanofibers. (a) TEM image of the longitudinal section of ZCO-600–5. (b) Elemental mapping along the longitudinal plane of ZCO-600–5. (c) HRTEM image of the region within the framed area in (a). (d) Lattice fringes and FFT of the *t*-ZrO_2 (200) crystallin plane shown in the insert. (e) TEM image of the cross section of ZCO-600–5. (f) Atomic resolution EDS mappings of (e). (g) Microstructure of the cross-section of ZCO-600–5. (h) STEM enlarged view of (g). (i) The STEM image in the Area 1 of (h). (j) Crystal order degree obtained after FFT transformation in the ZrO_2 crystallin phase region. (k) The STEM image in the Area 2 of (h). (l) Crystal order degree obtained after FFT transformation in the C phase of the Area 2.

and magnetic loss capacities can be quantitatively characterized by the dielectric loss tangent (tan $\delta_e = \varepsilon''/\varepsilon'$) and magnetic loss tangent (tan $\delta_m = \mu''/\mu'$), respectively. Both ZC and ZCO nanofibers are dielectric-dominated materials, with nearly constant μ_r values ($\mu' \approx 1$, $\mu'' \approx 0$) [27]. Therefore, dielectric loss constitutes the primary mechanism for electromagnetic energy dissipation in these materials, primarily encompassing conduction loss and polarization loss. Fig. 7 shows the frequency-dependent complex permittivity and dielectric loss tangent (tan δ_e) of both types of nanofibers [28]. Compared with ZC nanofibers, the introduction of low-permittivity ZrO_2 in ZCO nanofibers results in lower values of both ε' and ε'' (Fig. 7a and d) [29]. The gradual decrease in ε' with increasing frequency indicates typical dielectric dispersion behavior, suggesting the presence of dipole polarization [30,31]. This is primarily attributed to the relaxation that occurs when the dipoles within the sample fail to respond synchronously to the frequency variations of the alternating electromagnetic field [32]. According to Debye theory, ε'' is closely related to electrical conductivity [25]. The incorporation of ZrO_2 reduces the originally excessive electrical conductivity of ZC, leading to an overall decrease in ε''. The dielectric loss tangent are plotted in Fig. 7a and d. The ZC nanofibers exhibit a relatively high tan δ_e value, indicating their strong capability for dielectric loss [29]. To gain deeper insight into the internal dielectric loss mechanisms, the Cole-Cole semicircle trends for ZCO nanofibers are plotted according to the Debye theory and presented in Fig. S6, where each relaxation process corresponds to a semicircular arc, indicative of distinct dielectric relaxation events [33]. In the Cole-Cole plots (Fig. S6), all samples except ZCO-700–5 exhibit an extended tail in the low-frequency region, indicative of significant conduction loss resulting from high electrical conductivity [34]. Meanwhile, all samples display depressed semicircular arcs, revealing the coexistence of multiple polarization loss mechanisms in the nanofibers arising from various relaxation processes, including interfacial and dipolar polarization [35]. Interfacial polarization originates from the numerous heterogeneous interfaces induced by the Turing-like structures, whereas dipolar polarization is associated with defects and oxygen-containing functional groups introduced during the oxidation process. These defects serve as polarization centers, promoting dipole formation and subsequent polarization. Furthermore, under an alternating electromagnetic field, the oxygen-containing functional groups and inherent magnetic moments within the material undergo continuous oscillation and internal friction, thereby enhancing dipolar polarization loss [36].

The impedance matching characteristics and attenuation capabilities of EMW absorbing materials are of critical importance. The impedance matching characteristic is commonly evaluated using the normalized input impedance modulus ($|Z_{in}/Z_0|$), which can be calculated by Eq. (1). Generally, $|Z_{in}/Z_0|$ values ranging from 0.8 to 1.2 are

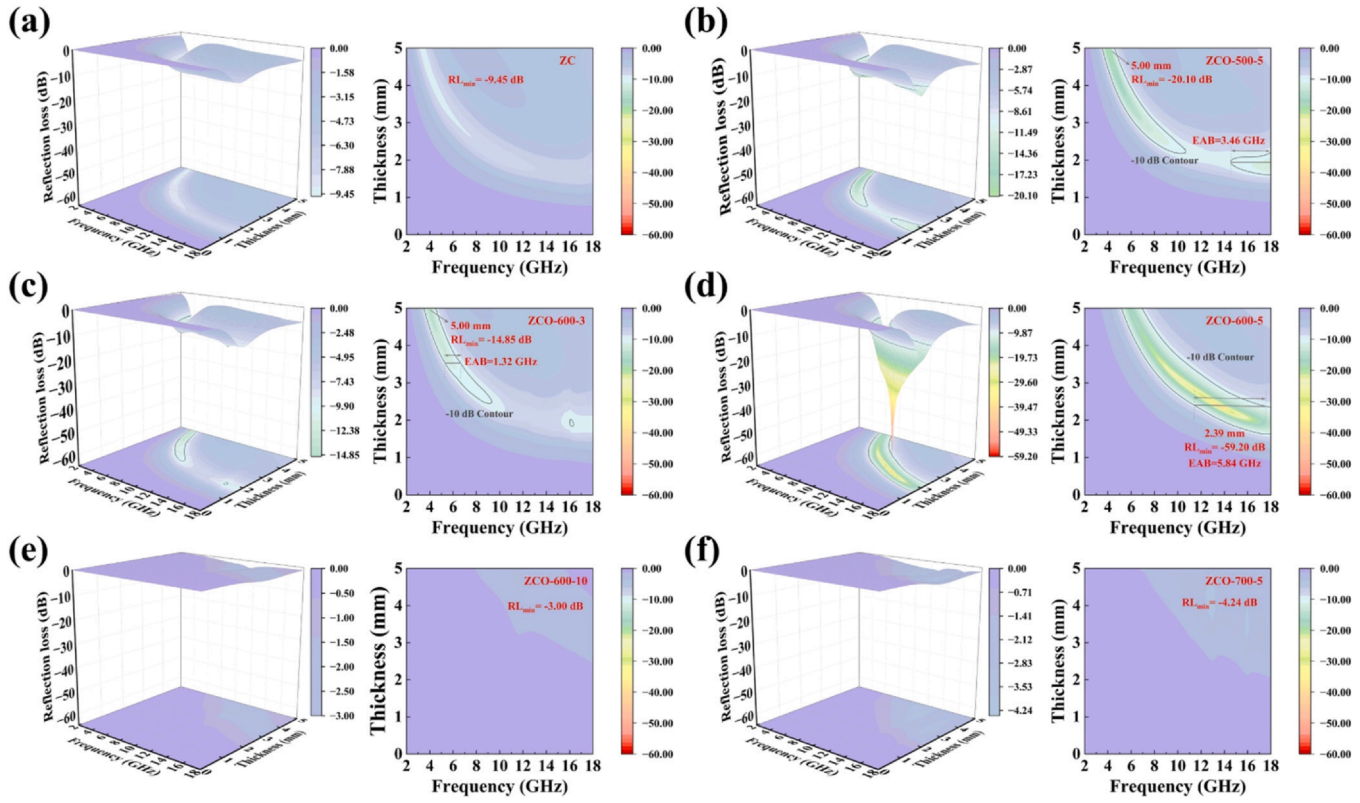

Fig. 6. 3D and 2D profiles of the theoretical reflection loss values. (a) ZC. (b) ZCO-500–5. (c) ZCO-600–3. (d) ZCO-600–5. (e) ZCO-600–10. (f) ZCO-700–5.

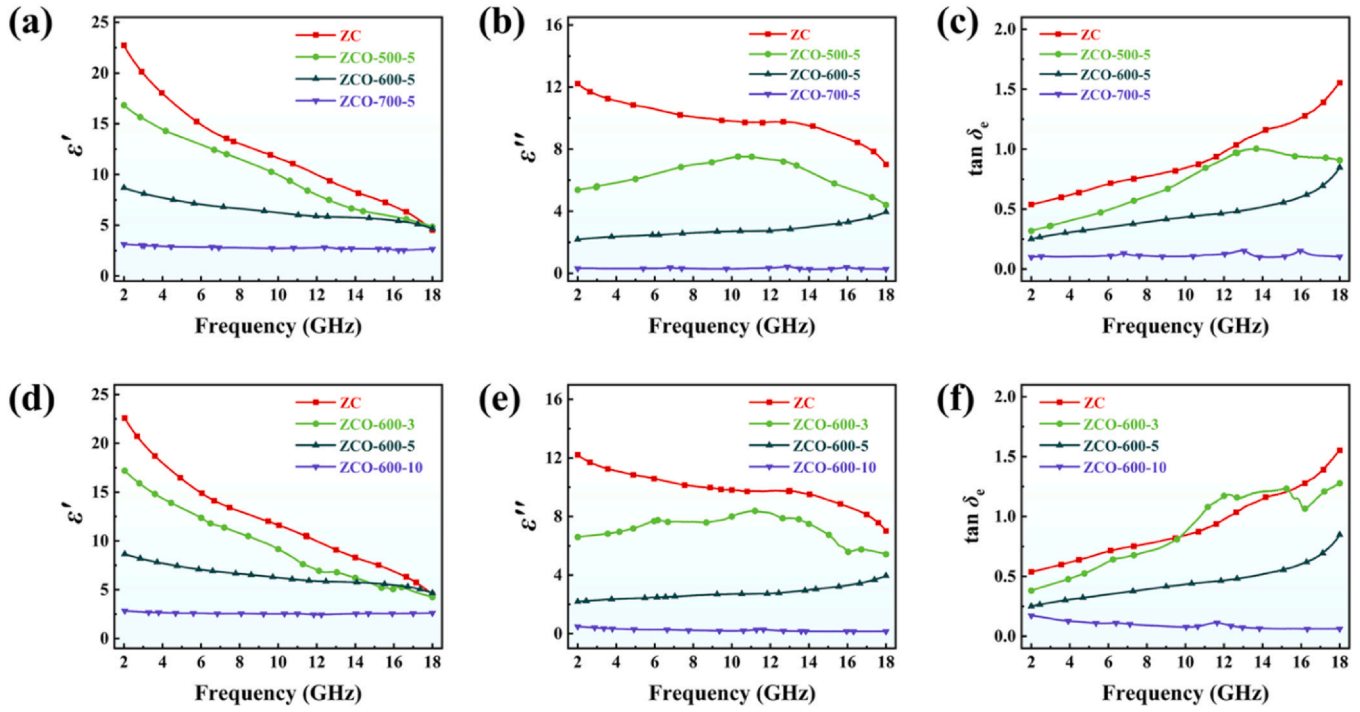

Fig. 7. The ε', ε'' and tan δ_e curves of nanofibers. (a)-(c) ZC and ZCO obtained at different oxidation temperatures. (d)-(f) ZC and ZCO obtained at different oxidation times.

considered optimal for achieving effective impedance matching [37]. When $|Z_{in}/Z_0|$ approaches 1, optimal impedance matching is achieved, indicating minimal reflection of EMWs at the material surface and maximum penetration into the material for dissipation. On the other hand, the attenuation constant (α) is used to quantify the ability to attenuate EMWs, as derived from Eq. (3).

$$\alpha = \frac{\sqrt{2}}{c}\pi f \times \sqrt{(\varepsilon'\mu' - \varepsilon''\mu'') + \sqrt{(\varepsilon'\mu' + \varepsilon''\mu'')^2 + (\varepsilon'\mu' - \varepsilon''\mu'')^2}} \quad (3)$$

Fig. 8a-f present the two-dimensional impedance matching ($|Z_{in}/Z_0|$) profiles of ZC nanofibers and ZCO nanofibers obtained under various oxidation conditions. Although the $|Z_{in}/Z_0|$ value exhibits an overall increasing trend with oxidation, this trend does not indicate that

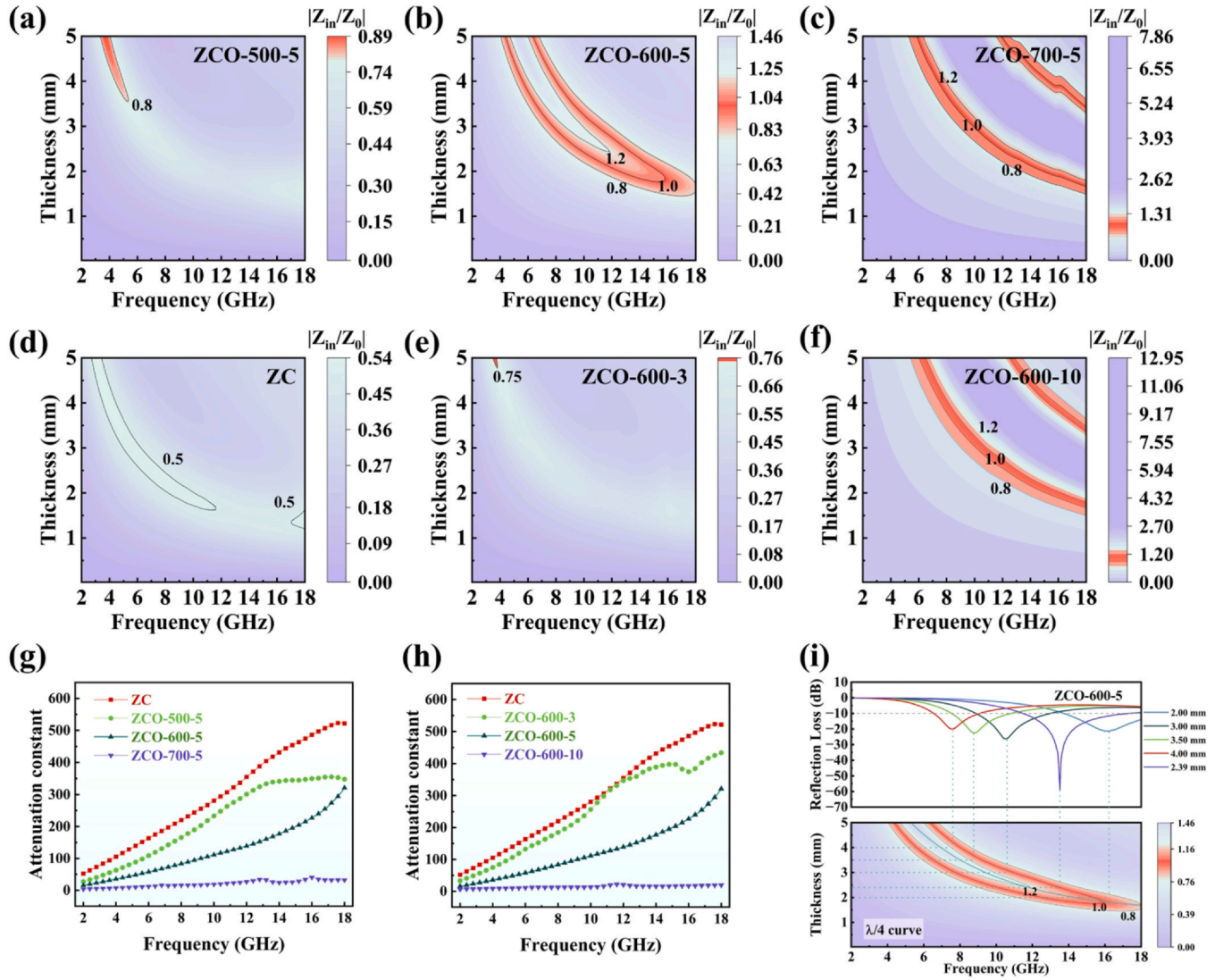

Fig. 8. Impedance matching, attenuation constant and quarter-wavelength curves of different nanofibers. (a)-(f) Impedance matching of ZC and ZCO. (g) Attenuation constants of ZC and ZCO obtained at different oxidation temperatures. (h) Attenuation constants of ZC and ZCO obtained at different oxidation times. (i) The $\lambda/4$ curve corresponding to the loss of ZCO-600–5.

excessive oxidation improves impedance matching. An increase in ZrO_2 content will enhance the penetration of EMWs into the material. For instance, the ZCO-700–5 sample exhibits a sharp decline in electrical conductivity due to increased ZrO_2 content and severe consumption of the carbon matrix. As a result, EMWs penetrate the material without being effectively absorbed. Moderate oxidation proves beneficial in optimizing impedance matching. As illustrated in Fig. 8b, ZCO-600–5 demonstrates excellent impedance matching characteristics, with $|Z_{in}/Z_0|$ approaching 1 across a broad frequency range. A large matching region is observed, and the bandwidth corresponding to the $|Z_{in}/Z_0|$ range of 0.8–1.2 reaches 5.92 GHz (11.4–17.32 GHz) at a specific thickness.

The attenuation constant (α) reflects the capability of a material to attenuate EMWs. As shown in Fig. 8h, the value of α exhibits a decreasing trend with the increasing oxidation degree. Although the ZC sample exhibits the highest attenuation constant (Fig. 8h), its poor impedance matching restricts overall absorption performance [38]. In contrast, the ZCO-700–5 sample exhibits the highest impedance matching and the lowest attenuation constant. As a result, EMWs can readily penetrate the material without being effectively absorbed [16]. Therefore, the key challenge lies in achieving a balanced control of $|Z_{in}/Z_0|$ and α for high-performance EMW absorption. The ZCO-600–5 sample exhibits optimal impedance matching and a moderate attenuation constant, the favorable synergy between these two factors endows the material with outstanding EMW absorption performance.

These findings indicate that the moderate introduction of amorphous and nanocrystalline ZrO_2 not only provides an effective means for tuning impedance matching but also, together with the Turing-like structure that enhances interfacial polarization via abundant heterogeneous interfaces, contributes to superior EMW absorption performance. Consequently, the superior EMW absorption performance of ZCO-600–5 is attributed to the synergistic effect of excellent impedance matching and moderate attenuation capability, ultimately achieving a wide effective absorption bandwidth and strong absorption performance, meeting the requirements for high-efficiency EMW absorption materials [39].

Furthermore, the absorption mechanism was analyzed using the quarter-wavelength theory (Fig. 8i). The calculation formula is presented in Eq. (4). This theory indicates that when the material thickness satisfies specific matching conditions, incident and reflected waves interfere destructively, converting electromagnetic energy into thermal energy. Compared with ZC nanofibers and other ZCO nanofibers samples (Fig. S7), the close agreement between the experimental matching

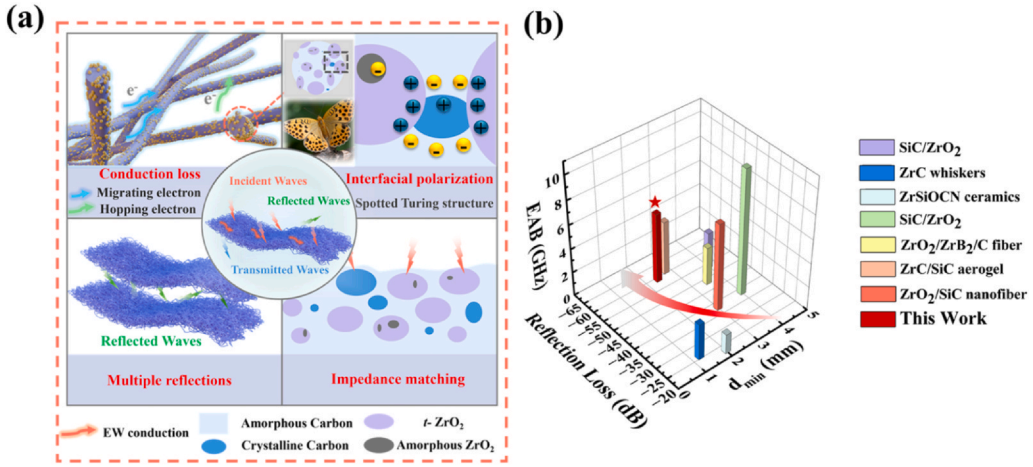

Fig. 9. Attenuation mechanism and comparison of EMW absorption performance among different materials. (a) Schematic illustration of the EMW attenuation mechanisms of ZCO-600–5. (b) Compression of *EAB* and *RL* of ZCO-600–5 sample with other published works [5,30,45–49].

thickness of ZCO-600–5 and theoretical predictions confirms the dominance of this mechanism [31].

$$t_m = \frac{n}{4}\lambda = \frac{nc}{4f_m\left|\sqrt{\varepsilon_r\mu_r}\right|}(n = 1, 3, 5, \ldots) \quad (4)$$

3.4. The microwave absorption mechanism and CST simulation

Fig. 9a provides a detailed summary of the EMW absorption mechanisms of the Turing-structured ZrO_2/C nanofibers. Firstly, the introduction of low-dielectric-constant ZrO_2 optimizes the impedance

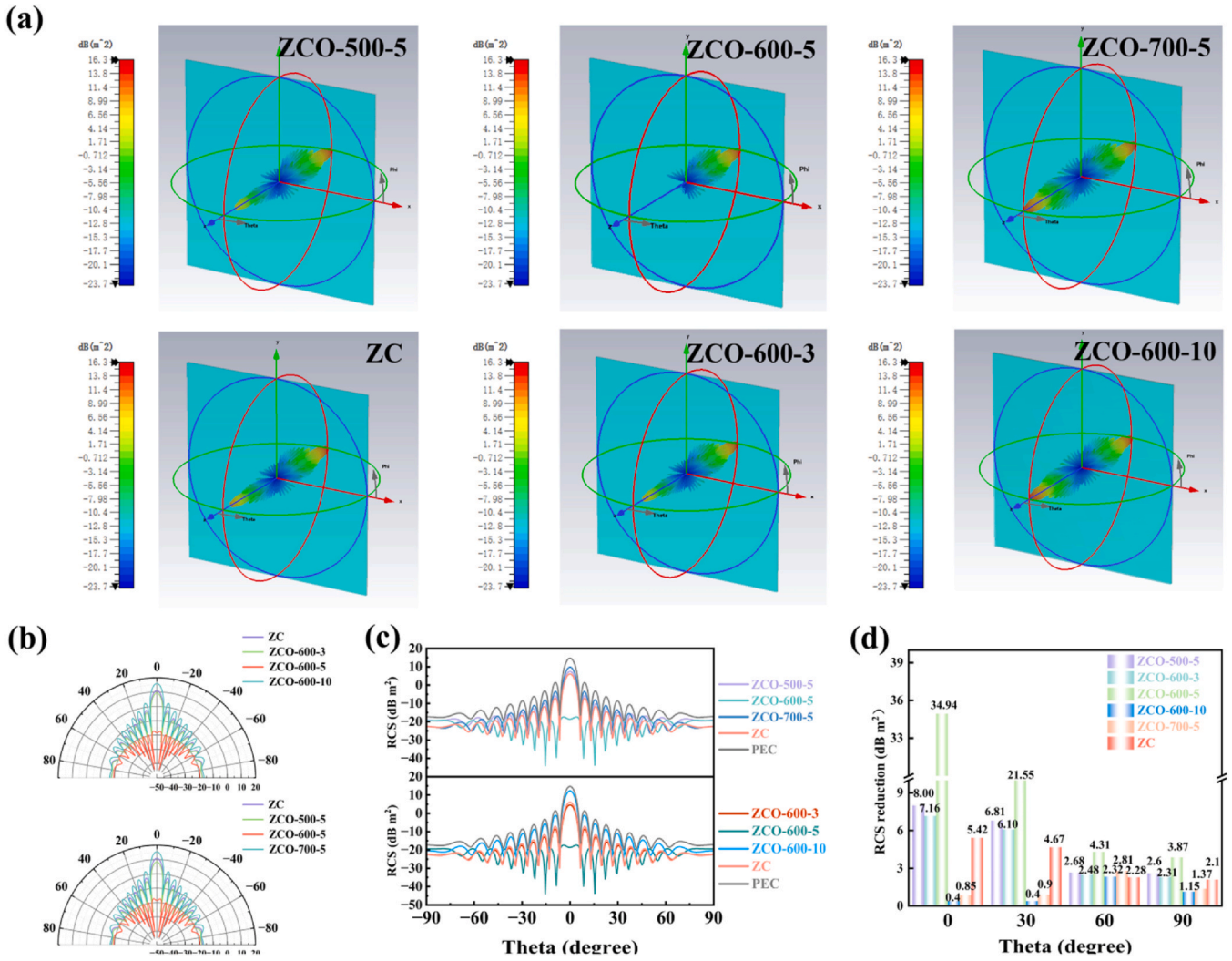

Fig. 10. CST simulation of different nanofibers. (a) Far-field simulation results of 3D CST for ZC and different ZCO samples. (b) RCS values (-90° < θ < 90°). (c) Simulated RCS curves (-90° < θ < 90°). (d) RCS reduction values at a thickness of 2.89 mm, 13.52 GHz and different scattering angles.

matching of the ZrO_2/C nanofibers by modulating the dielectric constant, allowing more EMWs to penetrate and be absorbed within the material. Secondly, the multi-scale 3D conductive network formed by the amorphous/nanocrystalline ZrO_2 and the carbon matrix nanofibers substrate facilitates electron hopping, thereby inducing conduction loss and converting EMW energy into Joule heat [40]. Finally, beyond the primary Turing structure comprising ZrO_2 particles embedded in the carbon matrix, the basic building units of the Turing structure (ZrO_2 grain and carbon matrix) exhibit an amorphous/nanocrystalline hybrid nature with abundant heterogeneous interfaces. These interfaces promote the accumulation and migration of free charges, significantly enhancing interfacial polarization and thus strengthening the dielectric loss capability of the nanofibers [41]. Moreover, the multi-scale heterogeneous nanofibers structure facilitates multiple reflections of EMWs, prolonging and increasing the propagation path of incident waves. In summary, the strategic compositional and structural design achieved a synergistic effect between optimized impedance matching and enhanced attenuation in the ZCO-600–5 sample, leading to exceptional EMW absorption performance, which surpasses that of most conventional nanofiber materials (Fig. 9b).

CST Studio Suite 2022 was employed to simulate the far-field radar wave interaction with the actual materials. A single-layer substrate model, comprising the sample coated on a Perfect Electric Conductor (PEC) base, was constructed (Fig. S8). The EMW absorption performance under practical application conditions was evaluated by comparing the reduction in radar cross-section (RCS) at various incident angles [42]. When the EMW-absorbing material is applied to a target surface, its strong absorption significantly attenuates the reflected RCS signal, indicating enhanced radar stealth capability [30,43]. As shown in Fig. 10a, with incident waves along the *Z*-axis, the RCS distribution intensity of the ZCO-600–5 sample is markedly lower than that of the ZC sample and those processed under other oxidation conditions (Fig. 10b), suggesting that ZCO-600–5 dissipates more incident EMW energy. This implies that in real-world scenarios, a larger proportion of radar waves would be absorbed by this material. The 2D radar imagery and corresponding RCS data (Fig. 10c and d) further confirm that ZCO-600–5 achieves the lowest RCS values, specifically demonstrating reductions of 34.94 dB m^2 at 0° and 21.55 dB m^2 at 30° incidence [44]. These simulation results are highly consistent with the measured EMW absorption properties, strongly demonstrating the excellent performance and promising potential of ZCO-600–5 for radar stealth applications.

4. Conclusions

In this study, ZrC (ZC) nanofibers prepared via electrospinning and carbothermal reduction were successfully transformed into a series of ZrO_2/C (ZCO) nanofibers with varying oxidation degrees through a controlled oxidation process. The EMW absorption properties and mechanisms of the nanofibers were systematically investigated. The appropriately oxidized ZCO nanofiber sample not only retained a Turing-type speckled structure with ZrO_2 grains embedded in the carbon matrix, but also exhibited a mixed amorphous/nanocrystalline state in both the ZrO_2 and carbon phases, generating abundant heterogeneous interfaces. EMW absorption measurements demonstrated that ZCO-600–5 achieved a minimum reflection loss (RL_{min}) of −59.20 dB at a thickness of 2.39 mm and a maximum effective absorption bandwidth (EAB_{max}) of 5.84 GHz, significantly outperforming the pristine ZC nanofibers and other samples oxidized under different conditions. The excellent performance is attributed to the incorporation of ZrO_2, which optimizes impedance matching and facilitates the penetration of EMWs into the material. Simultaneously, the multi-scale 3D conductive network constructed by the amorphous/nanocrystalline ZrO_2 and the carbon matrix successfully achieves synergistic optimization by maintaining excellent impedance matching while exhibiting superior conductive loss capabilities. Furthermore, Rich heterogeneous interfaces brought by Turing structures, considerably improving the dielectric loss capability. This work not only demonstrates the feasibility of tuning the electromagnetic characteristics of carbide-derived nanofibers through controlled oxidation, but also provides important theoretical insights for the design of high-performance EMW absorption nanofibers based on multiphase heterogeneous structures.

CRediT authorship contribution statement

Yaqing Li: Writing – original draft, Formal analysis, Data curation, Conceptualization. **Cheng Fang:** Writing – review & editing, Supervision, Project administration. **Bei Cai:** Resources, Investigation, Data curation. **Xu Long:** Writing – original draft, Formal analysis, Conceptualization. **Huimin Xiang:** Project administration, Formal analysis, Conceptualization. **Hailong Wang:** Supervision, Resources, Funding acquisition. **Yanchun Zhou:** Writing – review & editing, Supervision.

Declaration of Competing Interest

We declare that we have no financial and personal relationships with other people or organizations that can inappropriately influence our work, there is no professional or other personal interest of any nature or kind in any product, service and/or company that could be construed as influencing the position presented in, or the review of, the manuscript entitled **"Design of amorphous/nanocrystalline turing structures in ZrO_2/C nanofibers for enhanced microwave absorption performance"**.

Acknowledgement

This research was financially supported by the National Natural Science Foundation of China (No. U23A20562, 52172075, 52302074 and 52302066), the China Postdoctoral Science Foundation (No. 2021M702931), the Natural Science Foundation of Henan Province (No. 232300421323).

Appendix A. Supporting information

Supplementary data associated with this article can be found in the online version at doi:10.1016/j.exm.2026.100022.

References

[1] H.L. Lv, Z.H. Yang, H.G. Pan, R.B. Wu, Electromagnetic absorption materials: current progress and new frontiers, Prog. Mater. Sci. 127 (2022) 100946.
[2] L. Zhang, Y.S. Huo, Y. Liu, M.S. Zhao, Y.J. Tan, S.Y. Huo, L. Yao, S.H. Qu, Z.H. He, Design and synthesis of non-homogeneous CoS_2/carbon composite fibers for enhanced microwave absorption, Carbon 236 (2025) 120120.
[3] J.R. Guo, S.B. Fu, Y.P. Deng, X. Xu, S. Laima, D.Z. Liu, P.Y. Zhang, J. Zhou, H. Zhao, H.X. Yu, S.X. Dang, J.I. Zhang, Y.D. Zhao, H. Li, X.F. Duan, Hypocrystalline ceramic aerogels for thermal insulation at extreme conditions, Nature 606 (7916) (2022) 909.
[4] H. Zhu, X.L. Weng, M. Liao, J. Zheng, M. Bi, ZrO_2-interface-engineered SiC nanofiber aerogel with integrated hydrophobicity, thermal insulation, and broadband electromagnetic wave absorption, Appl. Surf. Sci. 711 (2025) 164079.
[5] X.N. Wang, L.P. Liu, X.P. Wang, X.J. Bai, J.G. Qin, X.X. Li, B. Wang, Joule heat induced ultrafine ZrO_2/C composites for enhanced microwave absorption, Surf. Interfaces 51 (2024) 104818.
[6] J.S. Im, J.G. Kim, T.S. Bae, Y.S. Lee, Effect of heat treatment on ZrO_2-embedded electrospun carbon fibers used for efficient electromagnetic interference shielding, J. Phys. Chem. Solids 72 (10) (2011) 1175–1179.
[7] Z. Tan, S.F. Chen, X.S. Peng, L. Zhang, C.J. Gao, Polyamide membranes with nanoscale Turing structures for water purification, Science 360 (6388) (2018) 518–521.
[8] K.R. Song, S.B. Wu, X.S. Shan, S.Y. Huang, G.D. Zhao, D.Y. Zhao, Fabrication and characterization of ZrC nano-ceramics derived from a single-source precursor and its feasibility as ZrC/C fibers in structure and function, Ceram. Int. 48 (23) (2022) 35011–35022.
[9] X.Y. Tao, S.X. Zhou, J.E. Ma, Z.M. Xiang, R.L. Hou, J.J. Wang, X.Y. Li, A facile method to prepare ZrC fibers by electrospinning and pyrolysis of polymeric precursors, Ceram. Int. 43 (4) (2017) 3910–3914.

[10] X.Y. Liu, Z.K. Zhang, F.Y. Wu, F.Y. Tian, J. Sheng, M.G. Li, J.M. Li, W.W. Yang, Y.S. Yu, Insight of multi-polarization effect by constructing high-entropy spinel ferrite/perovskite @ amorphous carbon for enhancing electromagnetic wave absorption, Chem. Eng. J. 516 (2025) 164053.
[11] J. Gong, B. Michalkiewicz, X.C. Chen, E. Mijowska, J. Liu, Z.W. Jiang, X. Wen, T. Tang, Sustainable conversion of mixed plastics into porous carbon nanosheets with high performances in uptake of carbon dioxide and storage of hydrogen, Acs. Sustain. Chem. Eng. 2 (12) (2014) 2837–2844.
[12] K. Zhao, F. Ye, L.F. Cheng, R.Z. Liu, J. Liang, X. Li, Synthesis of embedded ZrC-SiC-C microspheres via carbothermal reduction for thermal stability and electromagnetic wave absorption, Appl. Surf. Sci. 591 (2022) 153105.
[13] Q. Li, G.M. Shi, N. Wang, Q. Guo, M.Q. Geng, Y.X. Dai, Y. Qi, B.W. Zhang, Shell layer oxygen vacancies enhance the microwave-absorbing properties of TiN@CN/WO_{3-x} multiple heterogeneous materials, Diam. Relat. Mater. 157 (2025) 112485.
[14] M. Jin, B. Xu, J. Ma, C.C. Yi, Y.F. Liu, Manipulating the surface oxygen vacancies of the nanosized ZrO_2 carrier for Co-catalyzed Fischer-Tropsch synthesis, ACS Sustain. Chem. Eng. 13 (9) (2025) 3741–3751.
[15] Z.L. Hou, X.S. Gao, J.Y. Zhang, G.S. Wang, A perspective on impedance matching and resonance absorption mechanism for electromagnetic wave absorbing, Carbon 222 (2024) 118935.
[16] J. Qiao, X. Zhang, C. Liu, Z.H. Zeng, Y.F. Yang, L.L. Wu, F.L. Wang, Z. Wang, W. Liu, J.R. Liu, Facile synthesis of MnS nanoparticle embedded porous carbon nanocomposite fibers for broadband electromagnetic wave absorption, Carbon 191 (2022) 525–534.
[17] K. Wang, K. Zhao, Q.N. Meng, X. Li, Q. Bai, H. Jiao, Y.F. Tang, Preparation of zirconium carbide nanofibers by electrospinning of pure zirconium-containing *polymer*, Ceram. Int. 48 (17) (2022) 25474–25483.
[18] H. Zhang, Y.P. Zhao, X. Yang, G.L. Zhao, D.M. Zhang, H. Huang, S.T. Yang, N.X. Wen, M. Javid, Z. Fan, L.J. Pan, A facile synthesis of novel amorphous TiO_2 nanorods decorated rGO hybrid composites with wide band microwave absorption, Nanomaterials 10 (11) (2020) 2141.
[19] B. Li, G.F. Xu, L. Fu, Y. Li, J.W. Huang, Crystal growth by ordered coalescence of lattice arrays in ZrO_2-based nanocomposites at the early stage of crystallization, Mater. Charact. 168 (2020) 110573.
[20] Y.Q. Liang, H.Z. Cheng, Y.J. Zhang, J.Y. Jin, Y. Wang, J. Gu, J. Yang, Y.S. Li, Amorphous Zr-MOFs derived high-quality ZrC nanoparticles to prepare ZrC ceramics, J. Eur. Ceram. Soc. 45 (12) (2025) 117447.
[21] S. Zhang, X.H. Wang, C. Zhang, H.M. Xiang, Y.W. Li, C. Fang, M.L. Li, H.L. Wang, Y.C. Zhou, Microstructure, elastic/mechanical and thermal properties of $CrTaO_4$: a new thermal barrier material, J. Adv. Ceram. 13 (3) (2024) 373–387.
[22] H.Y. Luo, J.C. Cao, The epitaxial growth of TiC on ZrC in low-carbon steel, Mater. Sci. Tech. Lond. 38 (11) (2022) 730–733.
[23] G.R. Yang, B. Wen, Z.Y. Zhou, S.L. Wang, H.Y. Zhao, S.J. Ding, W. Yan, Flexible cobalt nanoparticles/carbon nanofibers with macroporous structures toward superior electromagnetic wave absorption, J. Colloid Interf. Sci. 636 (2023) 194–203.
[24] J.X. Cui, Q. Luo, Z.G. Zhang, J.C. He, Q.Z. Yang, B.L. Shen, Reversing relaxation-induced embrittlement by high-temperature thermal cyclic annealing in Zr-based metallic glass, J. Mater. Res. Technol. 30 (2024) 9148–9157.
[25] W.T. Yang, Y.Y. Xie, S.M. Xu, G. Wu, Y.Z. Wang, Upcycling of polyvinyl chloride to porous carbon for high-performance electromagnetic wave absorption materials, Chem. Eng. J. 496 (2024) 154054.
[26] Y.X. Wang, W. Cui, Z.X. Li, L. Zhang, Y. Ren, X.X. Wu, Z.H. He, Y.S. Huo, Enhanced interfacial polarization of SiC/C nanofibers loaded with cobalt ferrite nanoparticles for improved electromagnetic wave absorption, Sci. China Technol. Sc. 68 (3) (2025) 1320201.
[27] Y.S. Huo, K. Zhao, P. Miao, J. Kong, Z.L. Xu, K. Wang, F.P. Li, Y.F. Tang, Microwave absorption performance of SiC/ZrC/SiZrOC hybrid nanofibers with enhanced high-temperature oxidation resistance, Acs. Sustain. Chem. Eng. 8 (28) (2020) 10490–10501.
[28] X.X. Zhang, M.Y. Hao, Y.G. Zhang, R.Z. Li, A.Q. Lin, Z.P. Shen, X. Qian, P. Xu, H.X. Peng, C.X. Zhu, H.Q. Song, Enhanced electromagnetic wave absorption performance in carbon fiber via continuous surface modification with layered double oxides, J. Alloy. Compd. 1022 (2025) 108816.
[29] X.Q. Yin, Y.Y. Wang, N. Pang, C.H. Liu, Y. Xu, M.J. Yu, C.J. Zhou, Ultralight, highly elastic ZrO_2/carbon fiber reinforced reduced graphene oxide aerogels with radar and infrared stealth capabilities, Compos. Part. BEng. 303 (2025) 112628.
[30] J.X. Liu, S. Lv, H.Q. Hao, H.R. Zhao, W.H. Wang, Q.H. Jing, S.Q. Yan, J. Guo, Z.J. Wang, Design of low-shrinkage SiC/ZrO_2 porous ceramic for broadband electromagnetic wave absorption, J. Alloy. Compd. 1016 (2025) 178852.
[31] S.K. Hou, Y. Wang, F. Gao, F. Jin, W.J. Liang, Z.Z. Ge, G.X. Bai, X. Peng, H. Yang, Construction of hierarchical SnO_2@SnS_2 nanostructures on carbon cloth as advanced microwave absorbers, J. Mater. Sci. Mater. El. 34 (32) (2023) 2144.
[32] Q.Y. Li, L.Y. Liu, Q. Zhang, H. Kimura, C.X. Hou, F.S. Li, X.B. Xie, X.Q. Sun, J. Zhang, N.N. Wu, W. Du, X.Y. Zhang, Heterogeneous interfaces in 3D interconnected networks of flower-like 1T/ 2H Molybdenum disulfide nanosheets and carbon-fibers boosts superior EM wave absorption, J. Colloid Interf. Sci. 671 (2024) 67–77.
[33] K.S. Cole, R.H. Cole, Dispersion and absorption in dielectrics I. Alternating current characteristics, J. Chem. Phys. 9 (1941) 341.
[34] J.H. Zhang, Q. Li, Y. Jia, Y. Wang, J. Yang, TiN nanoparticles-decorated SiOC ceramic fibers with electromagnetic wave absorption and optimized infrared stealth properties, J. Alloy. Compd. 1038 (2025) 182668.
[35] B.D. Li, Y.L. Deng, C. Liu, J. Qiao, S.Y. Hou, N. Wu, F. Wu, Z.H. Zeng, J.R. Liu, Rare earth oxides CeO_2 nanoparticle embedded magnetic carbon nanofibers for electromagnetic cooperation and efficient electromagnetic wave absorption, J. Mater. Sci. Technol. 217 (2025) 1–8.
[36] J. Qiao, X. Zhang, D.M. Xu, L.X. Kong, L.F. Lv, F. Yang, F.L. Wang, W. Liu, J.R. Liu, Design and synthesis of TiO_2/Co/carbon nanofibers with tunable and efficient electromagnetic absorption, Chem. Eng. J. 380 (2020) 122591.
[37] F.H. Xu, Y.X. Wang, F.C. Tang, X.L. Dai, Z.Y. Zhao, Y. Kong, X.D. Shen, G.F. Shao, Synergistic enhancement of structure and function in carbonaceous SiC aerogels for improved microwave absorption, Carbon 233 (2025) 119854.
[38] D.Q. Huang, X.Y. Zhang, J.F. Dai, Z.Z. Yuan, One-dimensional C/Co composite nanofibers derived from ZIF-67 with excellent wideband electromagnetic microwave absorption performance, Colloid Surf. A 707 (2025) 13910.
[39] J.H. Zhu, W. Wang, Q. Zhang, Y.N. Fan, L. Liu, J.H. Yan, J.Y. Yu, Constructing magnetic carbon nanofiber composites with magnetic-electric synergistic loss effects for efficient microwave absorption, Compos. Part. BEng. 302 (2025) 112551.
[40] X. Yang, B.H. Li, B.S. Lin, H. Wang, T. Zhu, X. Su, Y.Y. Gao, Z.L. Lei, P.A. Liu, Q.Q. Yu, L.G. Wang, Dielectric synergistic gradient metamaterials enable exceptional ultra-wideband microwave absorption and antibacterial properties, Carbon 232 (2025) 119813.
[41] Z.Y. Zhang, Y.H. Zhao, Z.H. Li, L.J. Zhang, Z.X. Liu, Z.K. Long, Y.J. Li, Y. Liu, R.H. Fan, K. Sun, Z.D. Zhang, Synthesis of carbon/SiO_2 core-sheath nanofibers with Co-Fe nanoparticles embedded in via electrospinning for high-performance microwave absorption, Adv. Compos. Hybrid. Mater. 5 (1) (2022) 513–524.
[42] H. Han, Z.C. Lou, Q.Y. Wang, L. Xu, Y.J. Li, Introducing rich heterojunction surfaces to enhance the high-frequency electromagnetic attenuation response of flexible fiber-based wearable absorbers, Adv. Fiber Mater. 6 (3) (2024) 739–757.
[43] I. Abdalla, A. Elhassan, S. Ali, M.Y.H. Saty, E. Adam, L.H. Zou, Q.Q. Ni, Z.Z. Xu, Impact of defect-rich carbon nanofibers combined with magnetic materials on broadband electromagnetic wave absorption and radar cross-section reduction, Small Struct. 6 (7) (2025) 2400624.
[44] J. Wang, M.J. Han, Y.N. Liu, Y. Xiang, C.B. Liang, X.G. Su, Y.Q. Liu, Multifunctional microwave absorption materials of multiscale cobalt sulfide/diatoms co-doped carbon aerogel, J. Colloid Interf. Sci. 646 (2023) 970–979.
[45] C.W. Yang, K.W. Li, M.G. Hu, X.Y. Li, M. Li, X.Y. Hu, Y. Li, Z.L. Huang, G.W. Meng, Flexible ZrO_2/ZrB_2/C nanofiber felt with enhanced microwave absorption and ultralow thermal conductivity, J. Mater. 11 (4) (2025) 100988.
[46] Y. Guo, Q. Song, L.L. Zhang, X. Yang, W. Li, F. Zhao, S.Y. Zhang, L.H. Qi, High-aspect-ratio ZrC whiskers: synthesis, growth mechanism and electromagnetic wave absorption properties, J. Mater. 9 (2) (2023) 235–243.
[47] S. Tang, X.M. Fan, Z.L. Jia, M.H. Li, F. Ye, J.M. Xue, Effect of annealing temperature on the microstructure, dielectric, and microwave absorption performance of precursor blends derived ZrSiOCN ceramics, Ceram. Int. 50 (1) (2024) 2211–2220.
[48] H.L. Xing, Q.P. Liu, L.G. Zhang, Y. Liu, M.Q. Hu, One-pot hydrothermal synthesis of MWCNT/ZrO_2 composites for enhancing electromagnetic wave absorption performance, Nano 15 (3) (2020) 2050034.
[49] B.J. Zhang, Z.W. Tong, X. Wang, X.H. Chen, X.D. Wen, C. Ma, Zirconium-modified hierarchical porous SiC-based nanofibrous aerogel with efficient electromagnetic waves absorption and thermal insulation properties, J. Eur. Ceram. Soc. 45 (1) (2025) 116808.